Proceedings of ASME Turbo Expo 2020
Turbomachinery Technical Conference and Exposition
GT2020
June 22-26, 2020, London, England

GT2020-14439

LARGE EDDY SIMULATION OF THE 7-7-7 SHAPED FILM COOLING HOLE AT AXIAL AND COMPOUND ANGLE ORIENTATIONS

Kevin Tracy[1], Stephen P. Lynch[2]

[1]Pratt & Whitney, East Hartford, CT
[2]Penn State University, University Park, PA

ABSTRACT

Shaped film cooling holes are used extensively for film cooling in gas turbines due to their superior performance in keeping coolant attached to the surface, relative to cylindrical holes. However, fewer studies have examined the impact of the orientation of the shaped hole axis relative to the main flow direction, known as a compound angle. A compound angle can occur intentionally due to manufacturing, or unintentionally due to changes in the main flow direction at off-design conditions. In either case, the compound angle causes the film cooling jet to roll up into a strong streamwise vortex that changes the lateral distribution of coolant, relative to the pair of vortices that develop from an axially oriented film cooling hole. In this study, Large Eddy Simulation (LES) using the Wall-Adapting Local Eddy Viscosity (WALE) model was performed on the publicly available 7-7-7 shaped film cooling hole, at two orientations (0°, 30°) and two blowing ratios (M=1, 3). Laterally-averaged film effectiveness was largely unchanged by a compound angle at a blowing ratio of 1, but improved at a blowing ratio of 3. For both blowing ratios, the lateral distribution of film was more uniform with the addition of a 30° compound angle. Both wall normal and lateral turbulent convective heat transfer was increased by the addition of a compound angle at both blowing ratios.

Keywords: Large Eddy Simulation, CFD, film cooling, compound angle, shaped film cooling

NOMENCLATURE

Ca	Compound angle
CRVP	Counter rotating vortex pair
D	Diameter of film hole, 6.78 mm
DR	Density ratio, ρ_c/ρ_∞
I	Momentum flux ratio, $\rho_c U_c^2/\rho_\infty U_\infty^2$
$\dot{m}_C$	Coolant mass flow rate
M	Blowing ratio, $\rho_c U_c/\rho_\infty U_\infty$
P	Pitch between cooling holes
Q	Q-criterion, second invariant of velocity gradient tensor
Re	Reynolds number
T	Temperature
TKE	Turbulent kinetic energy
U_∞	Mainstream time-averaged velocity
u	X component of velocity
v'T'	Correlated Y component velocity and temperature fluctuations
v	Y component of velocity
w'T'	Correlated Z component velocity and temperature fluctuations
w	Z component of velocity
X	Streamwise distance measured from hole trailing edge
Y	Wall-normal height measured from surface
Z	Lateral distance measured from center of hole trailing edge for Ca0 and from most downstream point for Ca30

Greek

η	Local adiabatic effectiveness
θ	Non-dimensional temperature, $(T_\infty-T)/(T_\infty-T_c)$
ρ	Density

Subscripts

c	Coolant
θ	Momentum thickness
∞	Mainstream

Superscripts

$\bar{}$	Laterally-averaged value
'	Fluctuating value
"	Coordinate centered about peak adiabatic effectiveness
+	Inner coordinates

INTRODUCTION

Film cooling is a common technology used in gas turbine engines to provide a layer of cool air that shields components from the hot mainstream gases. Numerous studies have been presented investigating the practical design and fundamental physical mechanisms of film cooling; the reader is referred to a comprehensive review by Bogard and Thole [1]. Shaped film cooling holes, so called because the exit of the hole has a non-circular form intended to diffuse or otherwise control the jet interaction with the mainstream, are reviewed by Bunker [2]. In general, shaped film cooling holes can significantly improve film cooling effectiveness at a given blowing ratio due to diffusion and lateral spreading of the jets. This study computationally models a publicly available shaped film cooling hole known as the 7-7-7 hole [3], since its lateral and forward expansion angles are 7°.

Modeling of film cooling is challenging due to the multi-scale, anisotropic nature of the turbulence generated in the hole and in the interaction of the jet with the mainstream flow. Two-equation formulations for turbulence modeling are generally inadequate to predict these effects, although due to a mutual offset of mispredictions, often the laterally-averaged film cooling is reasonably well predicted [4]. To better predict film cooling, researchers have used scale resolving simulations of increasing fidelity (but also computational cost): hybrid models which employ two-equation modeling near the wall and scale-resolving behavior away from the wall [5–7]; Large Eddy Simulation (LES) which resolves all scales above a filter (grid) size [8–13]; or Direct Numerical Simulation (DNS) which resolves all scales [14,15].

Injection of a jet into a crossflow generates several types of vortical structures: a horseshoe vortex around the leading edge of the injection; roller (hairpin) vortices on the windward and lateral sides of the jet; and hanging vortices between the jet and the adjacent wall [16]. In-hole vorticity can also develop depending on the length of the hole and how flow enters the hole. For jets parallel to the crossflow, these structures eventually merge into a pair of streamwise vortices known as the counter-rotating vortex pair (CRVP), which are largely responsible for decay of the film cooling downstream. Scale resolving methods have helped to understand important physics that lead to CRVP development. Tyagi and Acharya [8] showed hairpin vortices around the interaction of a jet issuing from a cylindrical hole into the mainstream, which developed into the CRVP and were important for the turbulent mixing of the jet. Sakai, et al. [10] investigated cylindrical film cooling over a range of blowing ratios (M) and found that the dominant vortical structures leading to CRVP development dramatically changed from low to high M. At low M, similar hairpin vortex features as found by Tyagi and Acharya [8] were noted, but at high M, hanging vortices were responsible for the CRVP.

Shaped holes, with their wider outlets and lower jet velocity at a given blowing ratio relative to cylindrical holes, also have reduced interaction with the mainstream and thus weaker CRVP [17]. LES simulations by Wang, et al. [18] found that a fan-shaped hole (only lateral expansions of the diffuser) reduced the size of the horseshoe vortex, and generated lower-amplitude fluctuations in the flow downstream of the jet. Fu, et al. [14] performed DNS simulations for a fan-shaped hole at low to moderate Reynolds numbers. At low Re, they found no horseshoe vortex and significant blowoff, but at high Re, the horseshoe vortex was present and the larger range of turbulent structures around the jet tended to shield it from freestream turbulence. Implicit LES modeling of the 7-7-7 shaped hole by Oliver, et al. [13] showed that there can be a significant separation in the diffuser at high blowing ratios. The gradient diffusion hypothesis for turbulent heat transfer that is a prime assumption of RANS models was shown to be inappropriate in the near-hole region.

Often film cooling holes can be oriented in a direction not aligned with the mainstream flow. This angle is referred to as a compound angle, and can occur intentionally due to machining access restrictions, or unintentionally if mainstream flow direction changes due to engine operating condition. The compound angle significantly changes the interaction of the jet with crossflow, where it generally forms a single strong streamwise vortex instead of the CRVP. This results in better lateral spreading of film [19–21] but also higher heat transfer coefficients that persist far downstream [22]. A comprehensive set of LES simulations of cylindrical holes by Li, et al. [23] investigated the effect of hole length to diameter (L/D) and direction of hole inlet flow. Very short L/D holes did not develop the single vortex, but very long holes had no contribution of in-hole vorticity to the streamwise vortex (all vorticity was from the shear layer between the jet and mainstream). Hole inlet flow orientations that produced the most uniform flow at the hole exit plane were correlated with best film performance.

Relatively fewer studies have investigated shaped holes at a compound angle. Brauckmann, et al. [24] found that laterally-averaged film cooling for a fan-shaped hole was not significantly changed by compound angle, but heat transfer coefficients were increased. A series of studies at the University of Texas on the 7-7-7 public shaped hole has investigated the effect of internal crossflow [25,26], as well as the nature of the approach boundary layer [27]. In general, internal crossflow distorts the in-hole velocity and the film cooling uniformity. Heat transfer augmentation of a compound angle shaped hole is significant for a hole in a laminar approach boundary layer, while a turbulent boundary layer is less sensitive but still augments heat transfer near the hole exit. Haydt and Lynch present a series of studies for the 7-7-7 hole at a range of compound angles from 0° to 60° [28,29]. Even for a compound angle of 15°, a large streamwise vortex is present, and it increases in strength with increasing blowing ratio and compound angle. The nature of the lateral spreading of the flow in the diffuser results in a weaker streamwise vortex near the windward side of the diffuser, which transports some coolant to the side of the main streamwise vortex.

The physics of a compound angle shaped hole are less well understood than for compound angle cylindrical holes, but appear to be somewhat different based on experiments.

However, the authors are not aware of any studies to date that have used scale-resolved simulations to model compound angle shaped holes. This paper describes large-eddy simulations of film cooling from the public 7-7-7 hole at two blowing ratios (M=1, 3) and two compound angles (0°, 30°). The simulations are compared to experimental data of Schroeder and Thole [3] and Haydt and Lynch [28,29].

METHODS

This numerical study examined the 7-7-7 public shaped film hole [3] shown in Figure 1, at both a 0° compound angle and a 30° compound angle with a blowing ratio of 1 and 3. Each case is defined in Table 1. Inlet conditions were chosen to match the test section from shaped film cooling experiments performed by Haydt and Lynch [28,29] and Schroeder and Thole [3,30,31].

To decrease the required solution time, a single film hole with periodic boundary conditions was modeled to simulate an entire film row with a pitch of P/D=6. A turbulent boundary layer velocity profile was specified over the main inlet face. To generate incoming boundary layer conditions comparable to the test facility used by Haydt and Lynch [28,29] and Schroeder and Thole [3,30,31], a 1.85 mm by 1.85 mm rectangular trip strip located near the domain entrance was included in the model. The trip strip was placed 518.45 mm (76.5D) upstream of the film hole and generated momentum thickness Reynolds numbers, shown in Table 1 (the experiments were at Re_θ=670). The efficacy of this approach is indicated in Figure 2. Three-dimensional vortex structures are identified by positive values of the Q-criterion, which is the second invariant of the velocity gradient tensor [32]. Figure 2 shows isosurfaces of Q=10,000s^{-2} depicting turbulent structures within the boundary layer downstream of the trip strip.

The time average mean streamwise velocity profile of the LES Ca0M1 generated boundary layer at X/D=-5.4 is compared in Figure 3 to Spalding's law and LDV experimental

Table 1: Summary of cases and their parameters

	Ca0M1	Ca30M1	Ca0M3	Ca30M3
Ca (deg)	0	30	0	30
D (mm)	6.78	6.78	6.78	6.78
Inclination Angle (deg)	30	30	30	30
$\dot{m}_c$ (kg/s)	0.082	0.082	0.247	0.247
M	1.0	1.0	3.0	3.0
I	0.83	0.83	7.5	7.5
P/D	6	6	6	6
U_∞ (m/s)	10.36	10.51	10.36	10.51
T_∞ (K)	300	300	300	300
T_c (K)	250	250	250	250
DR	1.2	1.2	1.2	1.2
Re_θ (X/D=-5.4)	1108	883	1112	906

measurements taken by Eberly and Thole [33]. The LES results overpredict u^+ through the boundary layer. Figure 4 compares the Ca0M1 fluctuating velocity profiles at X/D=-5.4 to boundary layer DNS results from Wu and Moin [34] and LDV measurements for u'^+ from Eberly and Thole. Similar to the trend for u^+, the LES results overpredict u'^+ through the boundary layer. The discrepancies in both the mean and fluctuating velocity profiles are driven by the underprediction of wall shear resulting from near wall prism layer aspect ratios up to 15. The aspect ratio was allowed to be elevated in the upstream boundary layer developmental section in order to limit overall domain cell count. The profiles for the boundary layers in the Ca0M3, Ca30M1, and Ca30M3 cases are similar to the Ca0M1 profiles shown in Figures 3 and 4. Despite the mismatch in wall shear magnitude, the LES generated boundary layers are representative of a turbulent boundary layer profile, so the incoming LES test conditions are comparable to the experimental conditions.

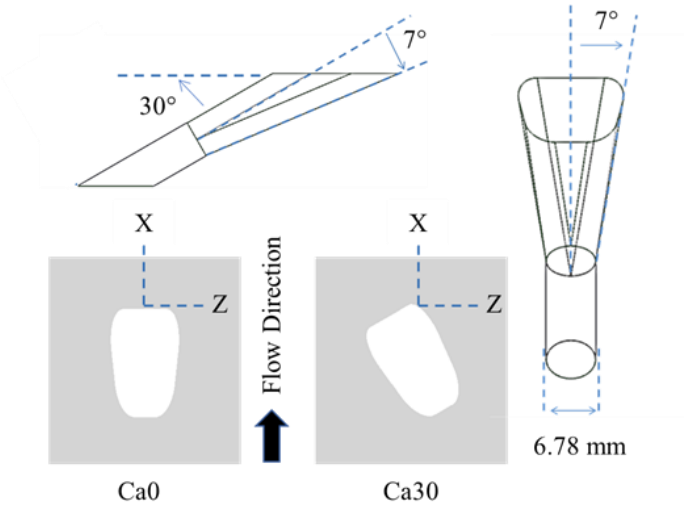

Figure 1: 7-7-7 public film hole designed by Schroeder and Thole [3], with compound angle by Haydt and Lynch [29].

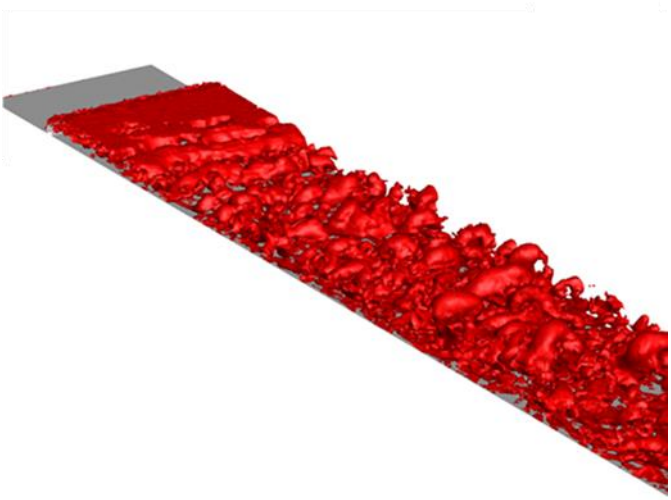

Figure 2: Q=10,000 s^{-2} isosurfaces depicting the upstream turbulent boundary layer development downstream of a trip.

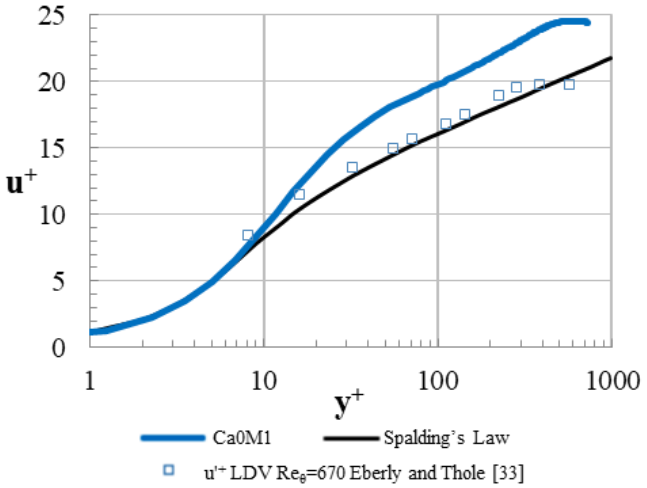

Figure 3: Mean streamwise velocity in inner coordinates at X/D=-5.4 for Ca0M1, and LDV measurements from Eberly and Thole [33], compared to Spalding's law.

The coolant inlet condition was specified as a fixed mass flow rate, listed in Table 1, and the domain exit was an outflow condition. Wall surfaces in the simulation were modeled as adiabatic.

Unstructured 3D polyhedral meshes were generated using StarCCM+ software [35]. Each case had 21 prism layers with near wall mesh spacing set such that the domain-average wall Y+ was 0.6. Boundary layer cell aspect ratio (lateral to wall-normal) was maintained below 15 throughout the domain. The resultant ΔX+ and ΔZ+ ranged from 0.3-28, with regions above 20 occurring in the boundary layer development region far upstream of the cooling hole. Global cell size was 0.2D and

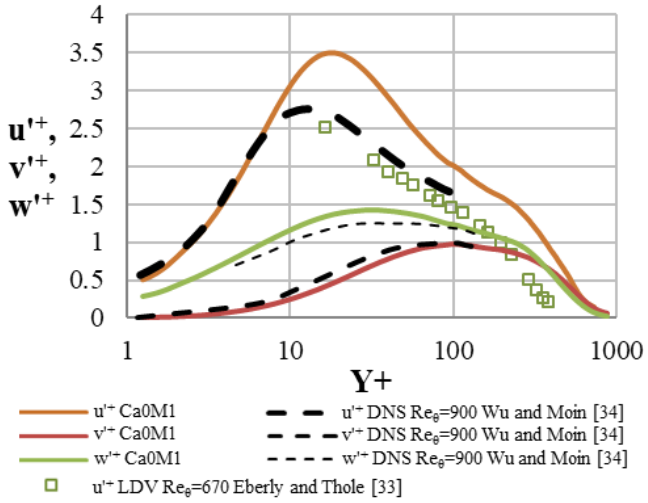

Figure 4: Fluctuating streamwise velocity in inner coordinates at X/D=-5.4 for Ca0M1, and LDV measurements from Eberly and Thole [33], compared to boundary layer DNS results from Wu and Moin [34].

refinement zones, with cell size as small as 0.015D, were used to concentrate cell density inside the hole and in the downstream region. Each mesh contained approximately 12 million cells. Figure 5 shows the computation domain for the 0° compound angle mesh, with the centerline of mesh overlaid.

To assess the resolution of the mesh, a resolved eddy viscosity was calculated from the mean flow field and fluctuating velocities and compared to the total eddy viscosity, which included the contribution from the sub-grid model. The ratio of resolved to total turbulent viscosity was greater than 99% when comparing Reynolds shear stresses to the associated mean velocity gradients in the eddy viscosity tensor.

The conservation equations were solved using Fluent V18.2 pressure-based solver with Wall-Adapting Local Eddy-Viscosity (WALE) subgrid-scale turbulence model [36,37]. The standard Fluent V18.2 specification for modeling constants were used [36]. Density and pressure were coupled using the incompressible ideal gas assumption, the SIMPLE algorithm was used to couple pressure and velocity, the spatial discretization of the advective terms of the Navier Stokes equations was bounded second-order central differencing, and the temporal scheme was bounded second-order implicit. The LES flow field was seeded from a steady RANS solution. After being seeded, the simulation was run for three flow-through times before data accumulation began, to assure that initial transient effects would not impact the time-averaged solution. The flow field data was averaged over six flow-through times (11,095 timesteps for M=1 cases and 22,190 timesteps for M=3 cases per flow-through) using a time-step of 8 microseconds and 20 inner iterations for Ca0M3 and Ca30M3, and a time-step of 4 microseconds and 16 inner iterations for Ca0M1 and Ca30M. This resulted in an average convective Courant number in the meter below 1.0 for the M=1 cases and 1.5 for the M=3 cases and a domain-average Courant number of 0.1 for all cases.

RESULTS

Comparisons to experimental flowfield and adiabatic effectiveness data of Haydt and Lynch [28,29] and Schroeder and Thole [3,30,31] are presented throughout this section, to validate the computational model. Also, the unique physics for compound angle shaped holes, including the first presentation of velocity-temperature correlation behaviors for compound angle shaped holes, are described.

Time-Average and Instantaneous Flow

The lateral spreading of film coverage is heavily influenced by the CRVP, which can be visualized by the normalized time-averaged streamwise vorticity. Experimental results for Ca0M3 from Haydt and Lynch [28] for a D=6.78mm and DR=1 (M=3, I=9) at X/D=5, and experimental results from Schroeder and Thole [30] for a D=7.75mm and DR=1.5 (M=3, I=6) at X/D=4, are compared against LES results from this study at X/D=5 in Figure 6. Unfortunately, there are not currently flowfield datasets for the 7-7-7 hole at a DR=1.2, which was one of the conditions common to the film cooling effectiveness datasets of Schroeder and Thole and Haydt and Lynch, that was replicated

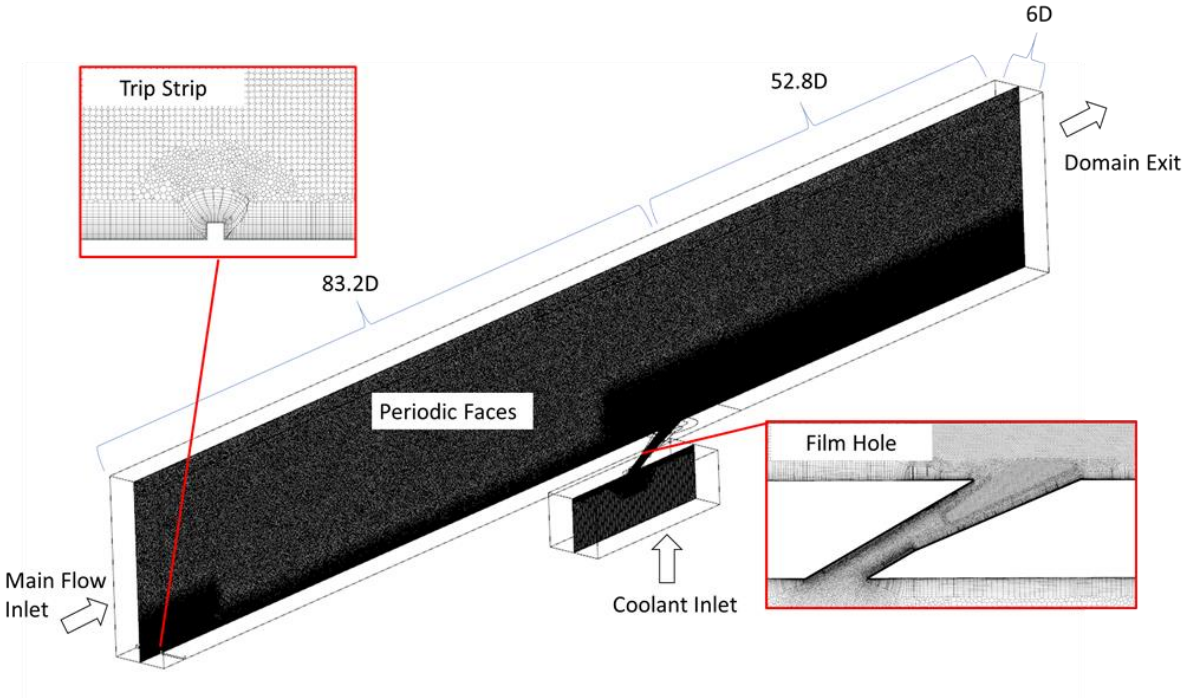

Figure 5: Computational domain with centerline of mesh shown.

in this study. All three results in Figure 6 show the CRVP cores at Z/D=±1. The magnitude of the LES calculated streamwise vorticity is within the range of the experiments, as would be expected due to the varying density ratios. The lower density ratio of Haydt and Lynch results in a higher momentum flux at the same blowing ratio, which causes the jet to lift further off of the endwall surface. Conversely, the high density ratio in Schroeder and Thole resulted in the jet remaining closer to the wall than in the present LES results. Generally, however, the flow trends are well predicted by the LES, in terms of the vorticity magnitude and the shape of the CRVP.

The introduction of a compound angle changes both the strength and symmetry of the CRVP, as seen in Figure 7 for a blowing ratio of 3 at X/D=0 for LES results. The Ca0M3 flow field shows weak, symmetric CRVP at Z/D=±1 and Y/D=0.5. The Ca30M3 flow field, Figure 7B, shows that the leeward vortex (positive vorticity) has become significantly stronger and has lifted further off the surface. This dominant vortex sweeps the cooling flow laterally which contributes to the more uniform coverage provided by the Ca30 film hole. In addition to enhancing lateral mixing, the dominant vortex increases the magnitude of the wall-normal velocity, which results in high velocity impingement toward the endwall occurring over the 1<Z/D<1.5. Heat transfer coefficient augmentation was not calculated in this study but may be augmented locally by this phenomenon [38].

The addition of a compound angle not only changes the vorticity at the hole exit, but also the decay and translation of vorticity with distance downstream of the cooling hole. By

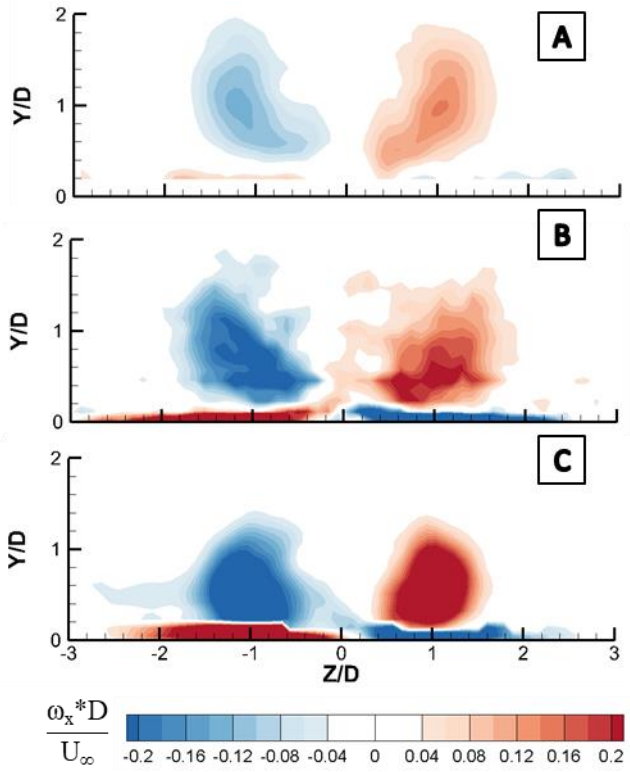

Figure 6: Comparison of mean vorticity to experimental data. A: Haydt and Lynch [28] at X/D=5 plane, B: LES at X/D=5 plane, C: Schroeder and Thole [30] at X/D=4 plane (no available flowfield data at X/D=5).

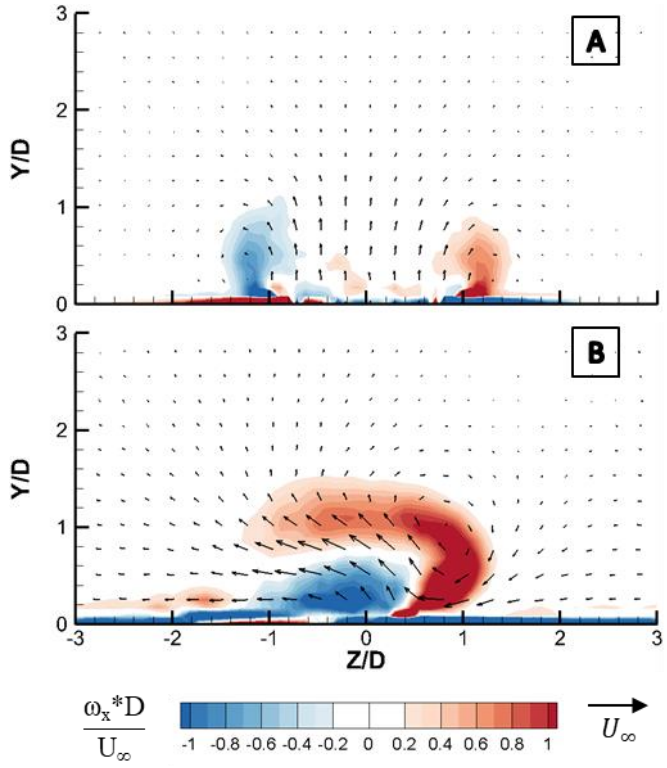

Figure 7: Normalized mean streamwise vorticity at X/D=0 plane for the LES simulations. A: Ca0M3, B: Ca30M3.

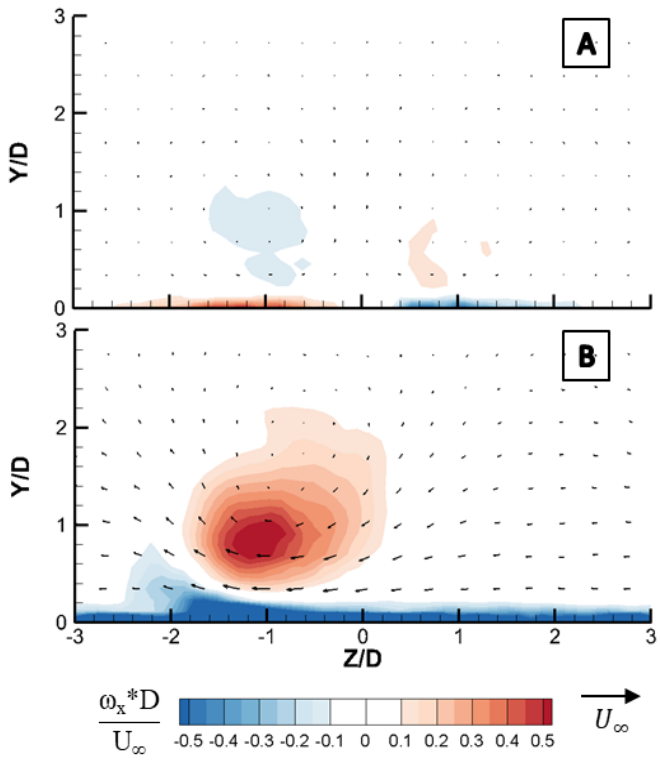

Figure 8: Normalized mean streamwise vorticity at X/D=10 plane for the LES simulations. A: Ca0M3, B: Ca30M3.

X/D=10, shown in Figure 8A, the vortex pair in the Ca0M3 case is still centered around Z/D=±1 and has decayed to low values of vorticity. In contrast, in the Ca30M3 case shown in Figure 8B, the dominant leeward vortex is still present at X/D=10 and the center of vorticity has been swept by the cooling jet laterally to Z/D=-1.

Figure 9 shows isosurfaces of Q=5E5 s^{-2}, colored by nondimensional fluid temperature, from the instantaneous velocity flow field for all four cases. The isosurfaces indicate local swirling features that are often assumed to represent fundamental vorticity elements that comprise the structure of a turbulent boundary layer. Note that the value of Q is arbitrary in terms of what features are highlighted, but here is consistent between the cases to indicate relative changes. Due to the turbulent nature of the approach boundary layer and the jet-mainstream interaction, it is difficult to distinguish a difference in turbulent structures emanating from the cooling hole or at the interface of the jet and free stream; however, some general trends are observed. The low momentum ratio for Ca30M1 results in the core of the jet being bent in the streamwise direction by the freestream so that it resembles the behavior of Ca0M1, while the higher momentum ratio in Ca30M3 allows it to maintain lateral velocity farther downstream. The tendency of the boundary layer hairpin vortices to be swept over the leading edge of the cooling hole from the windward to the leeward side is observed in animations of the flowfield for Ca30 cases (location identified with white arrows in Figure 9B and 9D), while in the Ca0 cases the upstream vortices did not typically traverse laterally over the upstream edge of the cooling jet.

Q-criterion isosurfaces of the mean flowfield, also colored by nondimensional flow temperature, are shown in Figure 10 and can be used to represent a time-averaged amalgamation of vortices. Horseshoe vortices around the leading edge of the hole breakout are present for all four cases, with larger vortices at the higher blowing ratios due to the additional blockage of the jet. For the Ca0M1 case in Figure 10A the 7-7-7 cooling hole is operating at close to optimal conditions in terms of lateral-averaged effectiveness for its geometry and density ratio [3] and has minimized the flowfield interaction to the point that the CRVP is not evident at the selected level of q-criterion. With the addition of a compound angle, the presence of a dominant vortex structure emanating from the leeward edge of the hole becomes apparent. It is stronger than the CRVP in Ca0M1 and transports some cooling away from the endwall, as is evidenced by its values of θ>0. At M=3 in Figure 10C, the obstruction caused by the jet is significant enough that the CRVP is clearly present for the Ca0M3 case. The strong CRVP tends to transport coolant away from the endwall, leading to θ>0 in the vortex legs downstream of the hole. For Ca30M3, a large amount of the coolant is entrained in the single streamwise vortex, which transports it relatively far downstream and provides some cooling to the wall, as will be shown in later adiabatic effectiveness results.

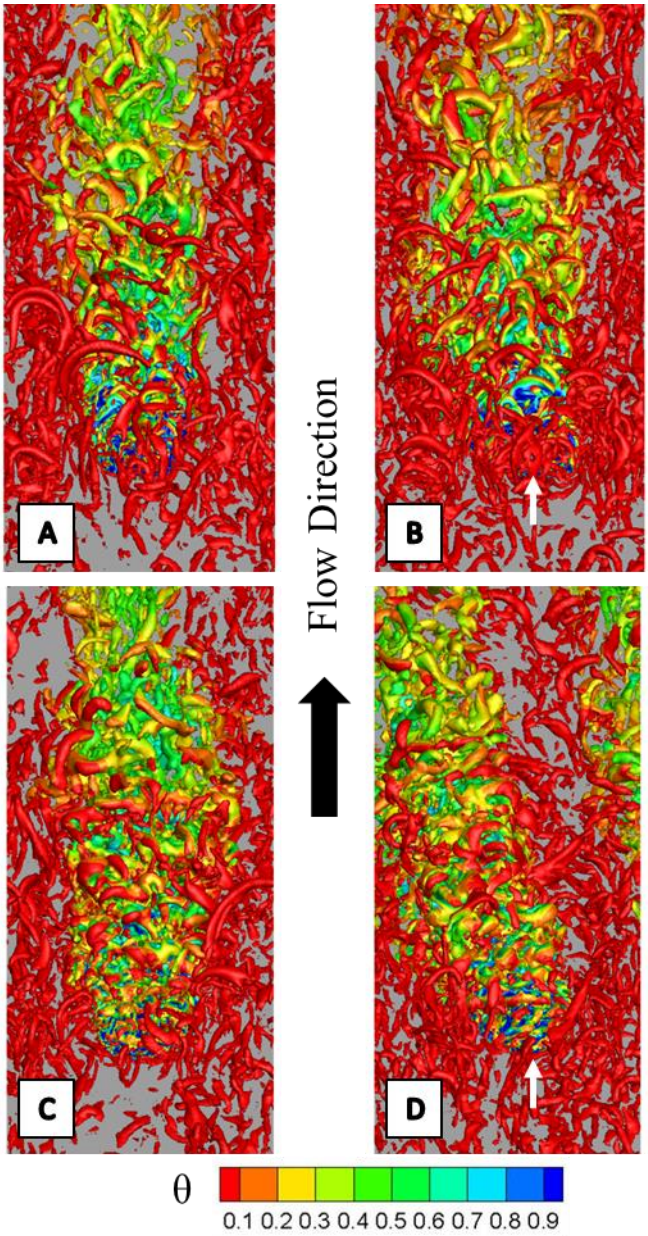

Figure 9: Instantaneous isosurfaces of Q=5E5 s^{-2} colored by nondimensional temperature: A: Ca0M1, B: Ca30M1, C: Ca0M3, D:Ca30M3.

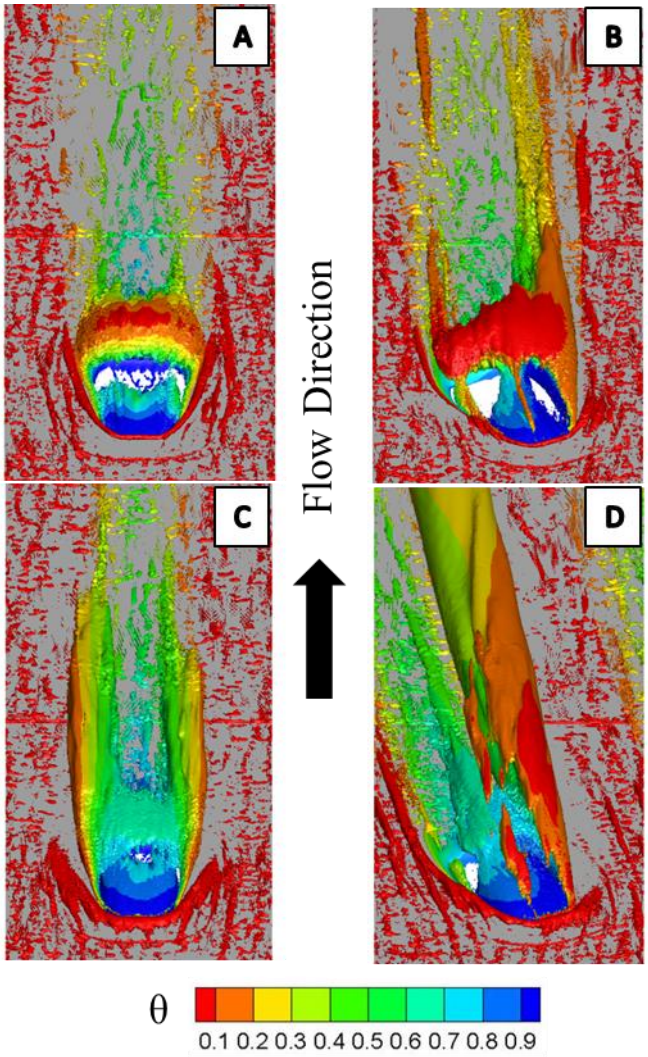

Figure 10: Q-criterion isosurfaces at 1E4 s^{-2}, calculated from the mean velocity and colored by nondimensional temperature: A: Ca0M1, B: Ca30M1, C: Ca0M3, D: Ca30M3.

Turbulent Flow

Turbulent velocity fluctuations augment the mixing between the cooling jet and the mainstream flow, but there is little information on how they differ between an aligned and a compound angle shaped hole. Figure 11 compares the fluctuating velocities of the LES at M=3.0 and DR=1.2, to the measured fluctuations by Haydt and Lynch [28], which were taken at a DR=1.0 (M=3.0, I=9.0). The figures are clipped to only show regions with values of TKE greater than 10% of the max in-plane TKE value, which indicates the region influenced by the film jet. In this figure, fluctuations are normalized by the local TKE for each case, to allow for comparison between the two slightly different momentum flux ratios. Interestingly, this choice of normalization shows reasonable agreement between the experiment and CFD, even though absolute values of nondimensional fluctuations (not shown) are different. Given that the magnitude of turbulent fluctuations are linked to the velocity ratio (momentum flux ratio), it seems reasonable that normalizing by TKE would appropriately scale the individual fluctuating components. Note also that this normalization is helpful in determining which of the three components contribute most to the local TKE at a given location.

In Figure 11 for Ca0M3, the fluctuations at the top of the jet are predominately in the wall-normal direction (v'), and the sides of the jet are dominated by lateral (w') fluctuations. These are associated with the roller vortices generated at the shear layer between the jet and mainstream. Also, clearly the turbulence in the jet is anisotropic, which is well known. The core of the jet, which contains turbulence generated from within the cooling

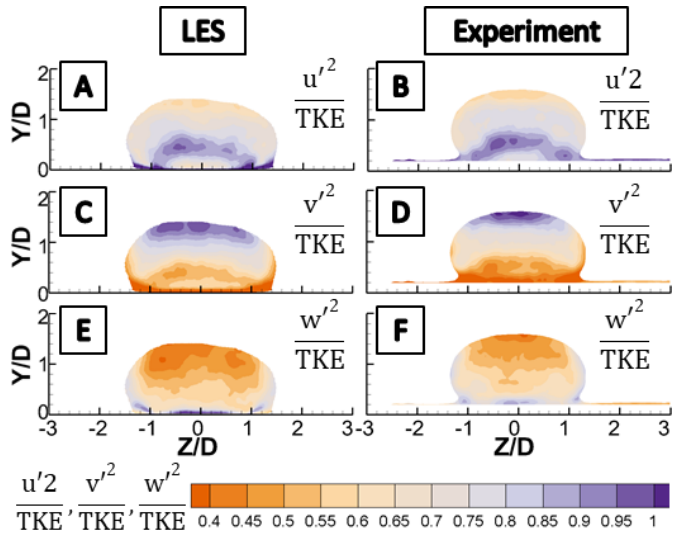

Figure 11: Comparison of squared fluctuating velocities normalized by local TKE at X/D=0 for Ca0M3, between this study (A,C,E) and Haydt and Lynch [28] (B,D,F).

hole, predominately consists of streamwise fluctuations with a lesser proportion of wall normal fluctuations.

For the Ca30M3 case in Figure 12, the fluctuating velocity components are asymmetrically distributed downstream of the hole, just as the mean flow is. Since the streamwise fluctuations in the core of the jet largely originate inside the hole, the distribution is somewhat comparable between the Ca30 and Ca0 cases, with perhaps slightly higher magnitudes for Ca30. The region where vertical fluctuations dominate (Figure 12C,D) is biased toward the leeward side of the jet, and has slightly higher magnitudes than in the Ca0M3 case. The lateral (w') fluctuations for Ca30M3 are concentrated primarily on the windward side of the jet, with much higher magnitudes than the Ca0M3 jet. This

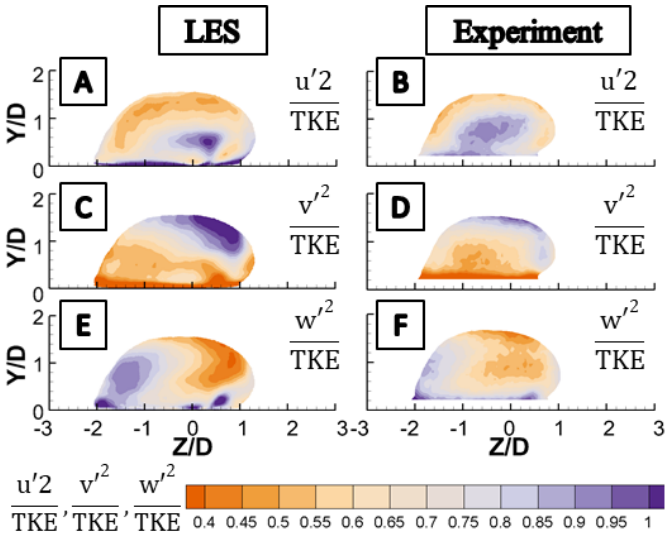

Figure 12: Comparison of squared fluctuating velocities normalized by local TKE at X/D=0 for Ca30M3, between this study (A,C,E) and Haydt and Lynch [28] (B,D,F).

suggests that the interaction of the streamwise vortex with the mainstream is quite unsteady on the windward side, and significant mixing likely occurs there. For Ca30M3 a secondary small, highly concentrated pocket of lateral fluctuations exists on the leeward side of the hole, near the wall, in line with the bottom of the dominant vortex seen in Figure 10D.

To compare normalized turbulent temperature fluctuations between Ca0M3 and Ca30M3 planes along the downstream edge of the cooling hole are used. For Ca0M3 this is the same as the X/D=0 plane that was previously used; for Ca30M3 the plane is shown in Figure 13. The Z/D=0 location remains consistent with the definition in Figure 1. Planes along the downstream edge of the hole are used in Figures 14 to 16.

Normalized turbulent temperature fluctuations at the downstream edge of the cooling holes are shown in Figure 14, overlaid with in-plane velocity vectors and nondimensional mean temperature isolines, where the bolded isoline of θ=0.1 indicates the time-mean edge of the cooling jet. For Ca0M3,

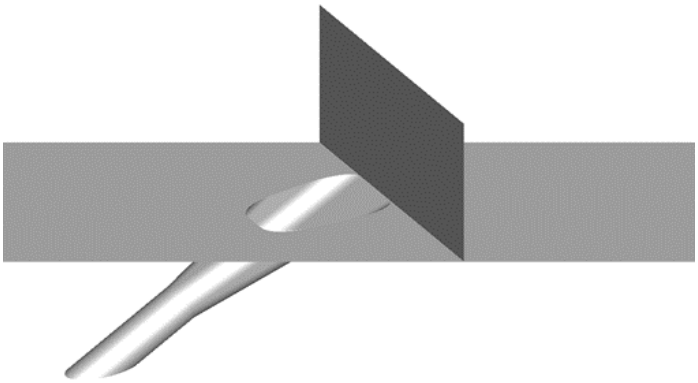

Figure 13: Ca30M3 plane along downstream edge used in Figures 14-16

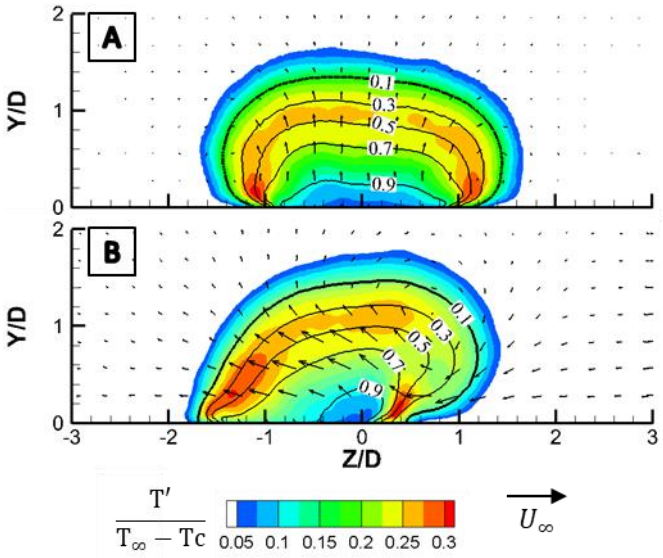

Figure 14: Comparison of normalized T' at the downstream edge of film hole footprint, overlaid with in-plane mean velocity vectors, non-dimensional mean temperature isolines, and a bolded θ=0.1 isoline, between A: Ca0M3 and B: Ca30M3.

localized symmetric peak temperature fluctuations occur near the wall along both edges of the jet where the CRVP is entraining hot gas under the coolant jet. High levels of temperature fluctuations also exist along the mean jet boundary as a result of mixing between the coolant jet and hot gases. The Ca30M3 case has a similar localized peak of high temperature fluctuations that occurs near the wall on the leeward edge of the hole (Z/D=0.5), where the dominant vortex is entraining hot gas under the coolant jet; however, the spatial extent of the high temperature fluctuations on the windward side at Z/D=-1.5 for Ca30M3 are greater than for the Ca0M3 case. This suggests that turbulent events on this windward side of the jet are more broadly distributed. Similar to Ca0M3, elevated temperature fluctuations exist along the boundary of the jet and the free stream.

Correlated velocity and temperature fluctuations are indicative of the turbulent transport of thermal energy, and are quite challenging to measure experimentally so there is little information in the literature about their structure. Figure 15 shows normalized v'T' from the LES simulations at the downstream edge of the cooling holes, with in-plane mean velocities and an isoline of θ=0.1 overlaid to indicate the mean coolant jet boundary. For the Ca0M3 case, v'T' is negative in the core and the top of the jet. As also indicated by Kohli and Bogard [39], this is likely due to the correlation between high temperature fluid moving downward to the wall, or low temperature fluid moving away which are the primary turbulent diffusion behaviors of the jet. However, the sides of the jet for Ca0M3 show positive v'T', which could correspond to the CRVP bringing cold fluid down to the wall. Note that other transport mechanisms (diffusion, dissipation) may also be important, but due to space constraints are not explored in detail here.

For Ca30M3 in Figure 15, both positive and negative v'T' zones are magnified in strength relative to Ca0M3, and like the mean flowfield, are asymmetrically distorted. The positive v'T' located at ~Z/D=1.5 in the Ca0M3 case has significantly reduced in size and been displaced downward to the wall by the enlarged and distorted negative v'T' region emanating from the jet core. The increased levels and area of elevated v'T' magnitude imply that turbulent thermal energy diffusion of the Ca30 jet will be somewhat higher than for Ca0.

Normalized lateral velocity-temperature correlations (w'T') are shown in Figure 16 at the downstream edge of the cooling

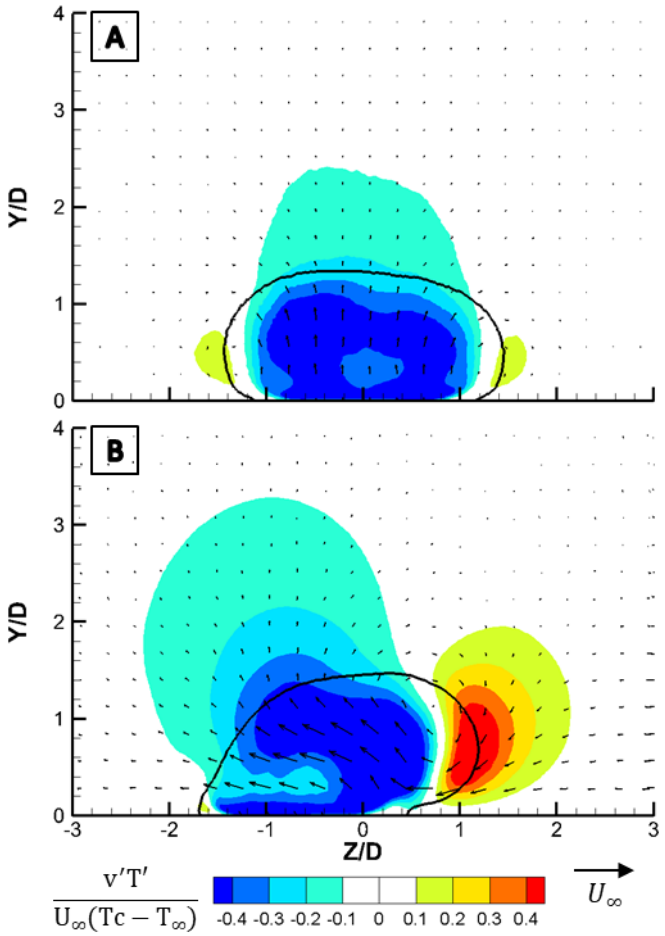

Figure 15: Comparison of normalized v'T' at the downstream edge of film hole footprint, overlaid with in-plane mean velocity vectors and θ=0.1 isoline, between A: Ca0M3 and B: Ca30M3.

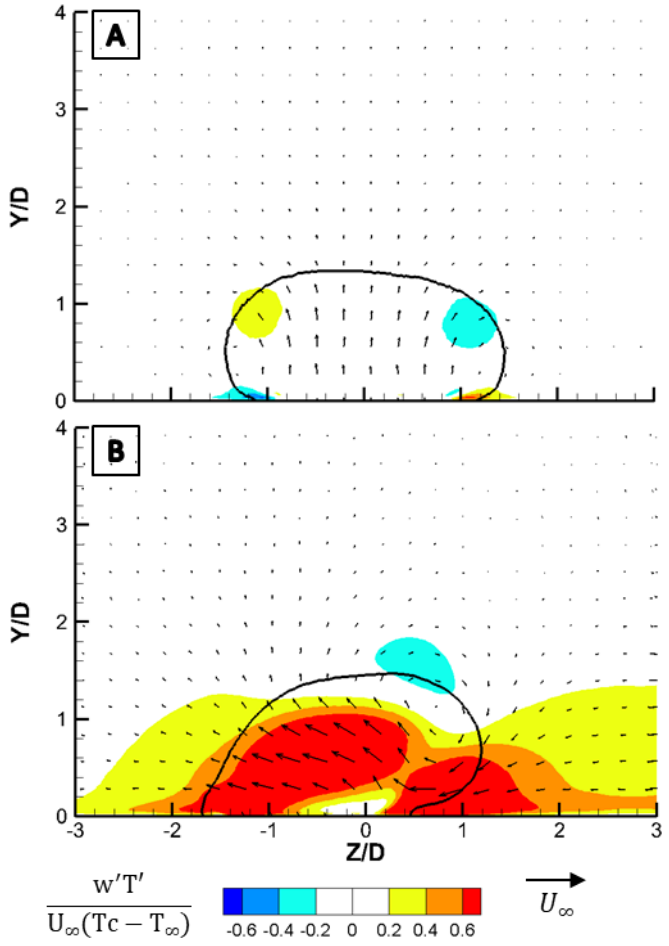

Figure 16: Comparison of normalized w'T' at the downstream edge of film hole footprint, overlaid with in-plane mean velocity vectors and θ=0.1 isoline, between A: Ca0M3 and B: Ca30M3.

holes. For the Ca0M3 case, the regions of high w'T' are of equal and opposite sign. This may be indicative of the effect of the CRVP: cold fluid is transported laterally out of the jet away from the wall (Y/D~1), while hot fluid is transported into the jet near the wall (Y/D~0). For the Ca30M3 case, there is only a small region of negative w'T' above the streamwise vortex, and the remainder of the plane has positive w'T'. Regions of large positive values of w'T' correspond to regions of strong mean Z-direction crossflow at Z/D=1.0; near the wall on the leeward side where the streamwise vortex is sweeping flow to the wall, and at Z/D=-1.0, near the windward side of the jet where it encounters the mainstream. The high positive w'T' along the endwall is indicative of low temperature fluid being transported laterally in the negative Z direction, which is connected to the improved lateral uniformity of film coverage discussed next.

Adiabatic Film Effectiveness

Laterally-averaged film effectiveness results from the current LES study, shown in Figure 17, were validated against experimental results from Schroeder and Thole [3] who collected endwall effectiveness data for Ca0M1 and Ca0M3 with DR=1.2 and D=7.75mm. At both blowing ratios the computational prediction is within the measurement uncertainty of ±0.024 from the experimental results, over nearly the entire length.

When comparing the laterally-averaged effectiveness between aligned and compound angle holes in Figure 17, the introduction of a 30° compound angle at a blowing ratio of 1 is seen to have negligible impact on lateral-average film effectiveness, due to minimal changes that occur in the flowfield. However, at M=3, the significant swirling vortex structures, seen in Figures 7 and 10, lift the Ca0M3 jet off of the surface and spread the Ca30M3 jet across the surface, resulting in improved laterally-averaged film coverage for Ca30M3 relative to Ca0M3.

Differences in lateral spreading of film between the 0° and 30° compound angle cases are shown in the contour plots of η in Figure 18. The addition of a non-zero compound angle results in the peak η not extending as far downstream, but with more laterally uniform film coverage. For the M=1 cases, this tradeoff between peak η and lateral spread results in a lateral-average that is the same for both compound angles, as described previously. For Ca0M3, the detachment of the jet and transport of cooling away from the wall by the CRVP manifests itself in a narrow η footprint. The introduction of a compound angle benefits cooling by replacing the CRVP with a dominant vortex, seen in Figures 10D and 14B, that sweeps laterally through the jet core, spreading it along the wall rather than lifting it.

The changes in lateral spreading are quantified in Figures 19 and 20, which plot the lateral film coverage at X/D=0 and 10, where Z"/D=0 is the location of maximum effectiveness for each case. In Figure 19, both Ca0M1 and Ca0M3 computational predictions show excellent agreement in lateral film distribution to experimental data from Schroeder and Thole [3] at X/D=0. At X/D=10 in Figure 20, there is also very good agreement in film distribution for Ca0M1 and Ca0M3 to experimental data, with some overprediction of η at the jet centerline (Z"/D=0) for Ca0M3.

At the hole exit (Figure 19), the peak η at M=1 is reduced slightly for a compound angle relative to an aligned hole, but the spread of film extends roughly 0.5D further in the -Z direction.

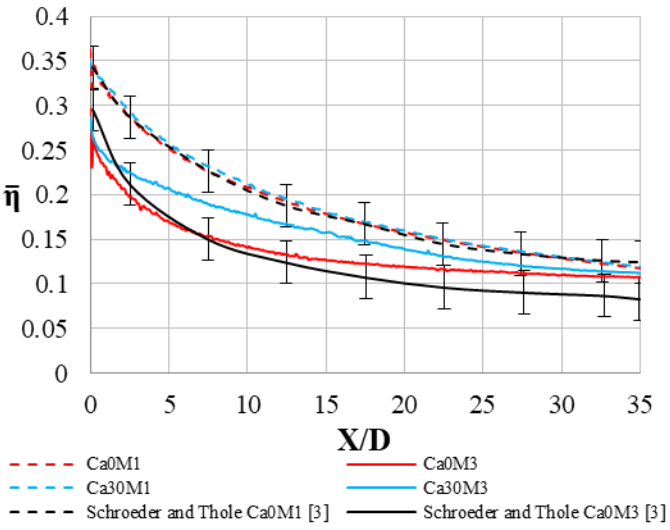

Figure 17: Laterally-averaged adiabatic effectiveness.

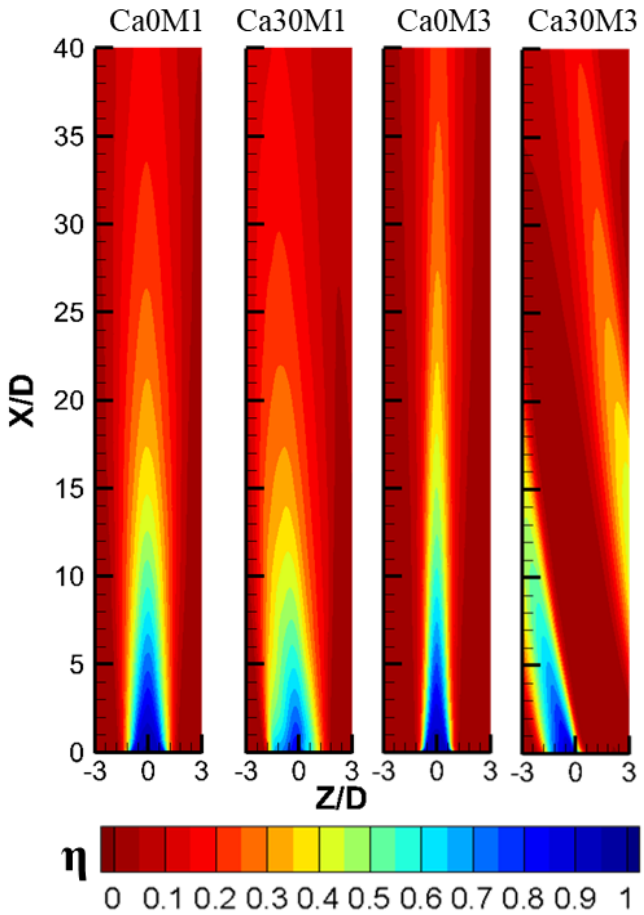

Figure 18: Computed adiabatic effectiveness contours.

For the higher blowing ratio of M=3, peak η at Z/D=0 is the same for Ca30M3 as it is for Ca0M3. Lateral coverage is improved near -1.5Z"/D and debited near 0.5Z"/D resulting in a net expansion of coverage by ~0.5D for Ca30M3 relative to the Ca0M3 configuration. Comparing the Ca0 cases it is seen that the elevated blowing ratio results in a symmetrically narrower film footprint caused by jet detachment and the CRVP counteracting lateral spread along the endwall. For the compound angle cases, however, elevated blowing ratio results in a narrower film footprint, but the narrowing mainly occurs on the leeward edge of the hole where the strong asymmetric vortex counteracts lateral spreading.

Figure 20 shows the trend of more uniform lateral coverage for a compound angled hole continues at X/D=10, as the film coverage extends ~0.5D further in the Z-direction for Ca30 cases relative to the Ca0 cases. The transport of the Ca30 jets by the streamwise vortex, as well as the enhanced lateral turbulent diffusion for a compound angle, as described in the flowfield section, allows film coverage to spread laterally over the first 10D, even though the jet is already more diffused at X/D=0.

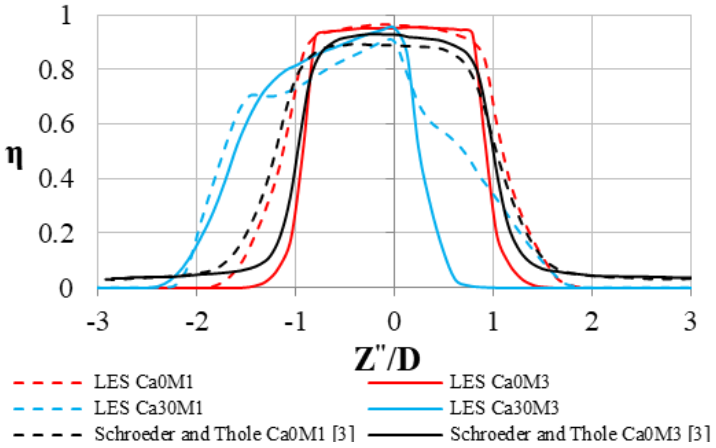

Figure 19: Lateral η distribution at X/D=0, where Z"/D=0 is the location of maximum effectiveness.

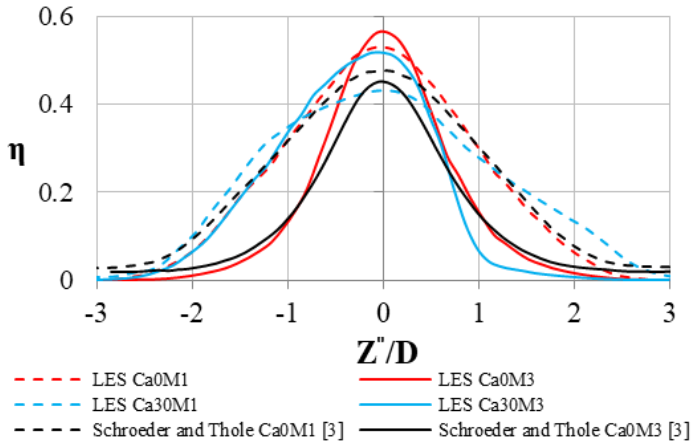

Figure 20: Lateral η distribution at X/D=10, where Z"/D=0 is the location of maximum effectiveness.

CONCLUSIONS

Large Eddy Simulations were conducted for the 7-7-7 shaped film cooling hole oriented at a 0° and a 30° compound angle, for blowing ratios of 1 and 3. Results for endwall film cooling effectiveness, streamwise vorticity, and turbulent fluctuating velocities were validated against experimental results with good agreement. Streamwise vorticity becomes asymmetric and stronger in magnitude with the addition of a compound angle. Wall-normal and lateral fluctuating velocity components are larger in magnitude for the compound angle relative to an aligned hole, as a result of increased mean in-plane velocity and the larger obstruction to the free stream.

Scale resolving CFD models are able to calculate temperature fluctuations and correlated velocity-temperature fluctuations which are difficult to experimentally measure, but critically important to understand for the thermal transport in the jet. The spatial extent of the temperature fluctuations is increased for compound angle film holes near the wall on the windward side of the hole (Z/D=-1.5), suggesting that turbulent events on this windward side of the jet are more broadly distributed. Lateral velocity-temperature fluctuations are higher, indicating better turbulent lateral spread of cooling for compound angle film. Laterally-averaged mean adiabatic effectiveness results show that average effectiveness is unchanged by the addition of a 30° compound angle for a blowing ratio of 1 and improved for a blowing ratio of 3, due to the strong crossflow generated by the streamwise vortex as well as augmented velocity-temperature fluctuations.

The dominant vortex generated by a non-zero compound angle may result in augmented local heat transfer coefficients depending on the film hole geometry, compound angle, and the flowfield, which can negate the improved coverage benefits. Further investigation is required to optimize a shaped cooling hole geometry for compound angle use, in order to obtain some of the benefits of improved lateral coverage and jet attachment at high blowing ratios while minimizing heat transfer coefficient augmentation. An optimization should ideally manipulate some of the physics investigated here.

ACKNOWLEDGEMENTS

The authors would like to acknowledge use of computational resources in the Advanced Cybercomputing Infrastructure at Penn State's Institute for Computational and Data Sciences. We would also like to acknowledge Pratt & Whitney for their support on this project.

REFERENCES

[1] Bogard, D. G., and Thole, K. A., 2006, "Gas Turbine Film Cooling," J. Propuls. Power, **22**(2), pp. 249–270.

[2] Bunker, R. S., 2005, "A Review of Shaped Hole Turbine Film-Cooling Technology," J. Heat Transfer, **127**(4), pp. 441–453.

[3] Schroeder, R. P., and Thole, K. A., 2014, "Adiabatic

Effectiveness Measurements for a Baseline Shaped Film Cooling Hole," *ASME Turbo Expo*, Düsseldorf, Germany, pp. 1–13.
[4] Hoda, A., and Acharya, S., 2000, "Predictions of a Film Coolant Jet in Crossflow With Different Turbulence Models," J. Turbomach., **122**(3), pp. 558–569.
[5] Foroutan, H., and Yavuzkurt, S., 2015, "Numerical Simulations of the Near-Field Region of Film Cooling Jets Under High Free Stream Turbulence: Application of RANS and Hybrid URANS/Large Eddy Simulation Models," J. Heat Transfer, **137**(1), pp. 1–12.
[6] Roy, S., Kapadia, S., and Heidmann, J. D., 2003, "Film Cooling Analysis Using DES Turbulence Model," *ASME Turbo Expo*, Atlanta, Georgia, USA, pp. 1–10.
[7] Kim, S. I., and Hassan, I., 2010, "Unsteady Simulations of a Film Cooling Flow from an Inclined Cylindrical Jet," J. Thermophys. Heat Transf., **24**(1), pp. 145–156.
[8] Tyagi, M., and Acharya, S., 2003, "Large Eddy Simulation of Film Cooling Flow From an Inclined Cylindrical Jet," J. Turbomach., **125**(4), pp. 734–742.
[9] Johnson, P. L., and Kapat, J. S., 2013, "Large-Eddy Simulations of a Cylindrical Film Cooling Hole," J. Thermophys. Heat Transf., **27**(2), pp. 255–273.
[10] Sakai, E., Takahashi, T., and Watanabe, H., 2014, "Large-Eddy Simulation of an Inclined Round Jet Issuing into a Crossflow," Int. J. Heat Mass Transf., **69**, pp. 300–311.
[11] Stratton, Z. T., and Shih, T. I.-P., 2018, "Effects of Density and Blowing Ratios on the Turbulent Structure and Effectiveness of Film Cooling," J. Turbomach., **140**(10), pp. 1–12.
[12] Guo, X., Schröder, W., and Meinke, M., 2006, "Large-Eddy Simulations of Film Cooling Flows," Comput. Fluids, **35**(6), pp. 587–606.
[13] Oliver, T. A., Anderson, J. B., Bogard, D. G., Moser, R. D., and Laskowski, G., 2017, "Implicit LES for Shaped-Hole Film Cooling Flow," *ASME Turbo Expo*, Charlotte, North Carolina, USA, pp. 1–14.
[14] Fu, W. S., Chao, W. S., Tsubokura, M., Li, C. G., and Wang, W. H., 2018, "Direct Numerical Simulation of Film Cooling with a Fan-Shaped Hole under Low Reynolds Number Conditions," Int. J. Heat Mass Transf., **123**, pp. 544–560.
[15] Muldoon, F., and Acharya, S., 2004, "Direct Numerical Simulation of a Film Cooling Jet," *ASME Turbo Expo*, Vienna, Austria, pp. 1–13.
[16] Fric, T. F., and Roshko, A., 1994, "Vortical Structure in the Wake of a Transverse Jet," J. Fluid Mech., **279**, pp. 1–47.
[17] Thole, K., Gritsch, M., Schulz, A., and Wittig, S., 1998, "Flowfield Measurements for Film-Cooling Holes With Expanded Exits," J. Turbomach., **120**(2), pp. 327–336.
[18] Wang, C., Zhang, J., Feng, H., and Huang, Y., 2018, "Large Eddy Simulation of Film Cooling Flow from a Fanshaped Hole," Appl. Therm. Eng., **129**(1), pp. 855–870.
[19] Schmidt, D. L., Sen, B., and Bogard, D. G., 1996, "Film Cooling With Compound Angle Holes: Adiabatic Effectiveness," J. Turbomach., **118**(4), pp. 807–813.
[20] Brittingham, R. A., and Leylek, J. H., 1997, "A Detailed Analysis of Film Cooling Physics: Part IV—Compound-Angle Injection With Shaped Holes," J. Turbomach., **122**(1), pp. 133–145.
[21] Lim, C. H., Pullan, G., and Ireland, P., 2013, "Influence of Film Cooling Hole Angles and Geometries on Aerodynamic Loss and Net Heat Flux Reduction," J. Turbomach., **135**(5), pp. 1–13.
[22] Sen, B., Schmidt, D. L., and Bogard, D. G., 1996, "Film Cooling With Compound Angle Holes : Heat Transfer," J. Turbomach., **118**(4), pp. 800–806.
[23] Li, W., Li, X., Ren, J., and Jiang, H., 2017, "Large Eddy Simulation of Compound Angle Hole Film Cooling with Hole Length-to-Diameter Ratio and Internal Crossflow Orientation Effects," Int. J. Therm. Sci., **121**, pp. 410–423.
[24] Brauckmann, D., and von Wolfersdorf, J., 2005, "Influence of Compound Angle on Adiabatic Film Cooling Effectiveness and Heat Transfer Coefficient for a Row of Shaped Film Cooling Holes," *ASME Turbo Expo*, Reno-Tahoe, Nevada, USA, pp. 1–9.
[25] McClintic, J. W., Klavetter, S. R., Winka, J. R., Anderson, J. B., Bogard, D. G., Dees, J. E., Laskowski, G. M., and Briggs, R., 2015, "The Effect of Internal Crossflow on the Adiabatic Effectiveness of Compound Angle Film Cooling Holes," J. Turbomach., **137**(7), pp. 1–10.
[26] McClintic, J. W., Anderson, J. B., Bogard, D. G., Dyson, T. E., and Webster, Z. D., 2018, "Effect of Internal Crossflow Velocity on Film Cooling Effectiveness—Part II: Compound Angle Shaped Holes," J. Turbomach., **140**(1), pp. 1–10.
[27] Anderson, J. B., Mcclintic, J. W., Bogard, D. G., Dyson, T. E., and Webster, Z., 2017, "Freestream Flow Effects on Film Effectiveness and Heat Transfer Coefficient Augmentation for Compound Angle Shaped Holes," *ASME Turbo Expo*, Charlotte, NC, USA, pp. 1–10.
[28] Haydt, S., and Lynch, S. P., 2018, "Flowfield of a Shaped Film Cooling Hole Over a Range of Compound Angles," *ASME Turbo Expo*, ASME, Lillestrom, Norway, pp. 1–15.
[29] Haydt, S., and Lynch, S., 2019, "Cooling Effectiveness for a Shaped Film Cooling Hole at a Range of Compound Angles," J. Turbomach., **141**(4), pp. 1–14.
[30] Schroeder, R. P., and Thole, K. A., 2016, "Effect of High Freestream Turbulence on Flowfields of Shaped Film Cooling Holes," J. Turbomach., **138**(9), pp. 1–10.
[31] Schroeder, R. P., and Thole, K. A., 2017, "Effect of In-Hole Roughness on Film Cooling From a Shaped Hole," J. Turbomach., **139**(3), pp. 1–9.
[32] Hunt, J. C. R., Wray, A. A., and Moin, P., 1988, "Eddies Streams and Convergence Zones in Turbulent Flows," *Proceedings of the 1988 Summer Program*, Stanford

University, CA, USA, pp. 193–208.
[33] Eberly, M. K., and Thole, K. A., 2014, "Time-Resolved Film-Cooling Flows at High and Low Density Ratios," J. Turbomach., **136**(6), pp. 1–11.
[34] Wu, X., and Moin, P., 2009, "Direct Numerical Simulation of Turbulence in a Nominally Zero-Pressure-Gradient Flat-Plate Boundary Layer," J. Fluid Mech., **630**, pp. 5–41.
[35] "STAR-CCM+" [Online]. Available: https://mdx.plm.automation.siemens.com/star-ccm-plus.
[36] ANSYS FLUENT, Release 18.2, Help System, Theory Guide, ANSYS, I., "Release 18.2."
[37] Nicoud, F., and Ducros, F., 1999, "Subgrid-Scale Stress Modelling Based on the Square of the Velocity Gradient Tensor," Flow, Turbul. Combust., **62**(3), pp. 183–200.
[38] Haydt, S., and Lynch, S., 2019, "Heat Transfer Coefficient Augmentation for a Shaped Film Cooling Hole at a Range of Compound Angles," *ASME Turbo Expo*, Phoenix, Arizona, USA, pp. 1–14.
[39] Kohli, A., and Bogard, D. G., 2005, "Turbulent Transport in Film Cooling Flows," J. Heat Transfer, **127**(5), pp. 513–520.